Simultaneous reconstruction of permittivity and conductivity using multi-frequency admittance measurement in electrical capacitance tomography

Maomao Zhang, Manuchehr Soleimani

Engineering Tomography Laboratory (ETL), Department of Electronic and Electrical Engineering, University of Bath, Bath, UK

Abstract

Electrical capacitance tomography (ECT) is an imaging method mainly capable of reconstructing dielectric permittivity. Generally, the reactance part of complex admittance is measured in a selected frequency. This paper presents for the first time an in depth and systematic analysis of complex admittance data for simultaneous reconstruction of both electrical conductivity and dielectric permittivity. A complex-valued forward model, Jacobian matrix and inverse solution are developed in the time harmonic excitation mode to allow for multi-frequency measurements. Realistic noise models are used to evaluate the performance of complex admittance ECT in a range of excitation frequencies. This paper demonstrates far greater potential for ECT as a versatile imaging tool through novel analysis of complex admittance imaging using a dual conductivity permittivity inversion method. The paper demonstrates that various classes of contactless capacitance based measurement devices can be analysed through complex multi-frequency ECT.

Keywords: Electrical capacitance tomography, complex value capacitance measurement, electrical admittance tomography, simultaneous reconstruction

I. Introduction

Electrical capacitance tomography (ECT) is an imaging method that reconstructs the permittivity distribution of dielectric materials. ECT is used as part of multiphase flow measurement [1-3], where the flow is normally of dielectric or low-conductive material. Some dual-modality imaging methods have been proposed for monitoring multiphasic flows. Combining ECT with a radiation-based imaging techniques has been proposed in [4-7], however this introduces radiation hazards and very high costs. ECT can be combined with Electrical Resistance Tomography (ERT) [7, 8]by using the conductivity reconstruction ability of ERT to provide more information.. This is limited because ERT needs a direct contact with the medium, requiring ERT electrodes to be mounted on the internal surface of the flow pipe/tube, increasing the cost for a dual modality ERT/ECT platform. For the conductive-background flow imaging, in [9], Zhang et al. introduced magnetic induction tomography (MIT) as a

support method to assist ECT in reconstructing the permittivity map. A dual ECT/MIT gives promising results in case of a dielectric background and as well as in the case of a conductive background, allowing the separation of two dielectric phases and a conductive phase. Both MIT and ECT are contactless methods. More work is still needed to establish MIT as a robust low conductivity imaging method [10]. In [11]capacitive coupling between MIT coils was investigated and highlighted a challenge in the interpretation of MIT data if phase changes are present due to capacitive coupling. In [12] a high frequency phase measurement method adapted from an MIT system was used to show capacitive coupled ECT measurement, referred to as electrical field tomography (EFT). This can be explained through the complex value ECT model presented in this paper.

In addition to multi-modal techniques, some single modality methods have been proposed: Electrical impedance tomography (EIT) can image complex impedance [13] but as in ERT direct contact with the conductive component of the imaging medium is needed. Reference [14] shows ECT imaging over a conductive medium, where the electrodes are in direct contact with the medium. This it is essentially the same as EIT and not contactless. In [15], a higher frequency excitation signal is introduced to help ECT to penetrate the conductive water, which is also of high permittivity, and produce more information about the permittivity distribution. In [16-18], a capacitively coupled ERT (CCERT) is used to image the conductivity distribution without contact with the conductive medium, without imaging the permittivity. Although various names are used, they are all can be analysed via complex-value multi-frequency capacitance tomography.

A multi-frequency method of contactless measurement and visualisation of both permittivity and conductivity is proposed in this paper. The aim is to investigate how much more information can be obtained from an ECT device assuming the complex admittance measurement is possible in a wide range of frequencies. A voltage excitation based admittance measurement is proposed and the receiving electrodes measure resulting complex-valued currents. A complex valued forward model, Jacobian matrix and inversion for ECT are presented in section 2. Image reconstruction results are shown in section 3, first for single frequency excitation with change of electrical conductivity of the background, and secondly for multi-frequency ECT measurement in a number of imaging scenarios. Summaries of the findings are presented in discussion and results sections.

2. Methods

A more in depth analysis of ECT with conductive background is critical. In this paper, we study perform a detailed of the relationship between the conductivity/frequency and permittivity and the capacitance measurements based on complex admittance measurements. By calculating the divergence of both sides of the Maxwell-Ampere equation, the following equation is obtained:

$$\nabla \cdot \left(\varepsilon(x) + \frac{\sigma(x)}{j\omega} \right) \nabla u(x) = 0 \quad \textbf{(1)}$$

$\varepsilon(x)$, $\sigma(x)$ and $u(x)$are the distributions of permittivity, conductivity and complexed value electric potential respectively, and ω is the angular frequency of the excitation signal. A complex capacitance forward model is solved using **equation (1)** and complex admittance is calculated. The equation below demonstrates the basic integral relation between complex capacitance and distribution of conductivity and permittivity [19]:

$$C = -\frac{1}{U} \int (\varepsilon(x) + \frac{\sigma(x)}{j\omega}) \nabla u(x) d\Gamma \quad \textbf{(2)}$$

where Γ is the surface of the electrode, U is the voltage on the electrode. Here C is a complex capacitance between pairs of electrodes. To ensure the validity of the complex value forward model, the in-house Matlab based software has been extensively verified against the commercial software COMSOL (https://www.comsol.com/) . First our standard real value ECT forward model was verified against the COMSOL forward model. After exact verification, this new complex value forward model was tested. In both cases our in house ECT software is in full agreement with the COMSOL forward model, which enables us to carry out these simulation studies with full confident.

ECT imaging is generally a time-difference based method, which means that the difference between two measurements at different times is used to calculate the change in permittivity distribution. In **equation (3)**, f is the mapping from the change in permittivity to the change in measurements.

$$\Delta C_{complex} = f(\Delta \varepsilon_{complex}) \quad \textbf{(3)}$$

Utilizing the finite element method, one can calculate the potential distribution inside the sensor and the capacitances for a given distribution of permittivity/conductivity using the complex-valued forward model. Furthermore, to obtain the distribution of permittivity/conductivity we need to calculate the sensitivity maps according to the fundamental perturbation theory (the change in capacitance in response to a perturbation of the permittivity or conductivity distribution):

$$J = \frac{\partial C_{complex}}{\partial \mathcal{E}_r} \ or \ \frac{\partial C_{complex}}{\partial \mathcal{E}_i} \quad \textbf{(4)}$$

Since the values in **equation (4)** are complex, this equation can be rewritten as below

$$J_{complex} \, \Delta \varepsilon_{complex} = \Delta C_{complex} \quad \textbf{(5)}$$

$$\begin{cases} J_{r,\varepsilon} \, \Delta \varepsilon_r + J_{r,\sigma} \, \Delta \varepsilon_i = \Delta C_r \\ J_{i,\varepsilon} \, \Delta \varepsilon_r + J_{i,\sigma} \, \Delta \varepsilon_i = \Delta C_i \end{cases} \quad \textbf{(6)}$$

where $C_{complex} = \frac{Y}{i\omega}$, Y is the complex admittance; C_r and C_i are the real and imaginary parts of $C_{complex}$; ε_r is the real permittivity value and ε_i is the conductivity divided by angular frequency of signal, $\frac{\sigma(x)}{\omega}$; $[J_{r,\varepsilon}, J_{r,\sigma}]$ and $[J_{i,\varepsilon}, J_{i,\sigma}]$ are the sensitivity maps linked the change in permittivity and conductivity to the real and imaginary part of capacitance change. **Equation (6)** can be expressed as the matrix format as:

$$\begin{bmatrix} J_{r,\varepsilon} & J_{r,\sigma} \\ J_{i,\varepsilon} & J_{i,\sigma} \end{bmatrix} \begin{bmatrix} \Delta\varepsilon_r \\ \Delta\varepsilon_i \end{bmatrix} = \begin{bmatrix} \Delta C_r \\ \Delta C_i \end{bmatrix} \quad \textbf{(7)}$$

Tikhonov regularization is used to calculate $\Delta\varepsilon_r$ and $\Delta\varepsilon_i$ in the equation above.

$$\begin{bmatrix} \Delta\varepsilon_r \\ \Delta\varepsilon_i \end{bmatrix} = \left(\begin{bmatrix} J_{r,\varepsilon} & J_{r,\sigma} \\ J_{i,\varepsilon} & J_{i,\sigma} \end{bmatrix}^T \begin{bmatrix} J_{r,\varepsilon} & J_{r,\sigma} \\ J_{i,\varepsilon} & J_{i,\sigma} \end{bmatrix} + \alpha I \right)^{-1} \begin{bmatrix} J_{r,\varepsilon} & J_{r,\sigma} \\ J_{i,\varepsilon} & J_{i,\sigma} \end{bmatrix}^T \begin{bmatrix} \Delta C_r \\ \Delta C_i \end{bmatrix} \quad \textbf{(8)}$$

Where I is the identity matrix and α is the regularisation factor. Through this equation, both the real and imaginary of permittivity can be obtained.

3. Results

3.1 Simulation of the capacitance measurements

As a time-difference imaging method, ECT needs two sets of capacitance: C_b, measurements of background scenario in **Figure 1(a)** and C_s, measurement of sample scenario **Figure 1(b)**. The relative permittivity of the water is set as $\varepsilon_{water} = 80$, and the conductivity is increased from 0 to 1 S/m. Frequency of the excitation voltage on the sensor is set at $f = 1.25$ MHz. A 12 external-electrode ECT device was considered with 66 independent measurements. An insulator layer of 0.5 *cm, i.e.*, the wall of the sensor, was considered with relative permittivity $\varepsilon_{wall} = 3$. The air sample is a circular region in diameter of 6 cm centred at (0, 3) cm. The simulation is to compute these two sets of capacitances through forward modelling. To obtain an accurate forward model, the finite element method bases on a dense mesh of 6552 elements, shown in **Figure 2(a)**.

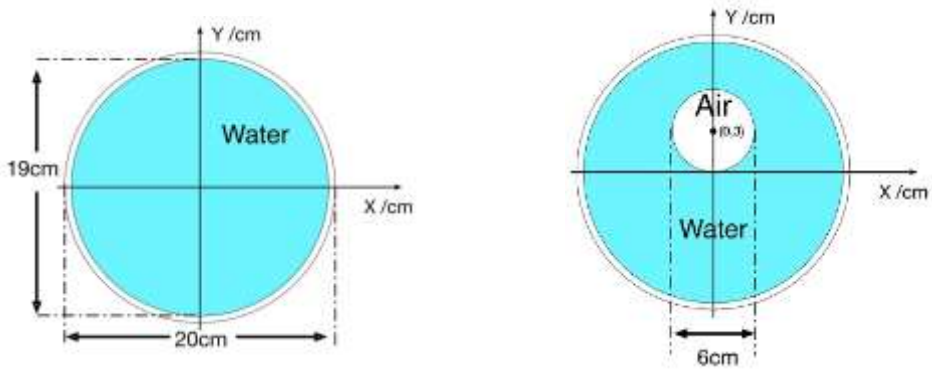

(a)Background: water filled sensor (b)Sample: Air in water

Figure 1. The dimensions of the ECT tank and the air sample

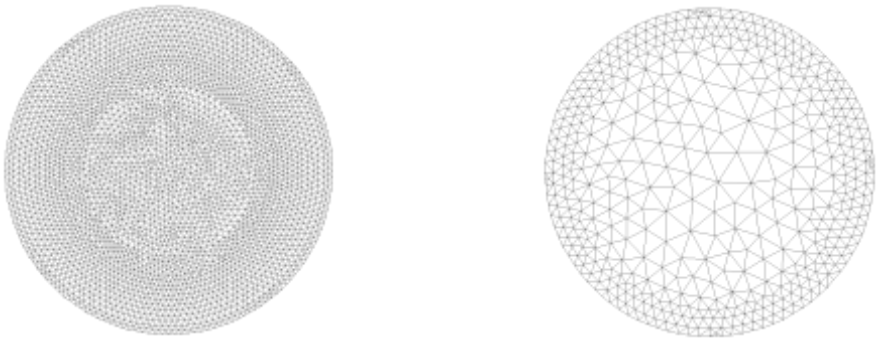

(a) Mesh of 6552 elements *(b) Mesh of 920 elements*

Figure 2. The FEM meshes: (a) the dense mesh for forward model simulation; (b) the coarse mesh for inverse problem solver.

To clearly indicate the trend of the capacitance change with increasing conductivity of background, both the real and imaginary parts of background and sample scenarios are plotted separately in Tables below.

In Table 1, the 66 inter-capacitance of every two electrodes are plotted. In the row of the background measurement, C_b, the permittivity/conductivity distribution is homogenous within the sensor. Therefore, the capacitance between the pairs of electrodes with equal spacing have the same magnitude and their plots overlap completely, then only six curves are shown, they stands for the capacitance between every neighbouring electrodes, every other electrodes, every three electrode *etc.*, till the opposite electrodes (every six electrodes). In the row of the sample measurement, C_s, the sample of air is added, which makes the electrical property distribution inhomogeneous. As a result, the 6 curves start to split.

To have a better understanding of the trend of complex capacitance, in Table 2, the 2-norm value of each set of 66 capacitance is plotted to describe the pattern of the capacitance change *verse* increasing conductivity.

Table 1. Real and imaginary part of every single inter-capacitance of any two electrodes

Capacitance	Real part	Imaginary part
C_b	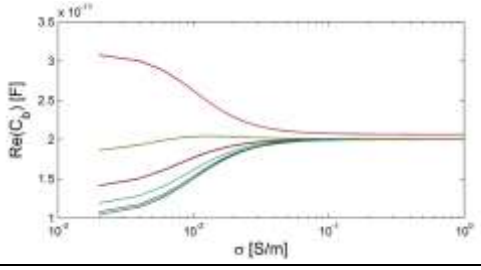	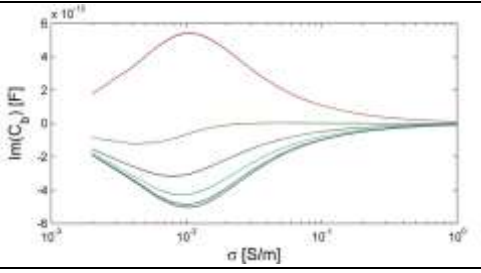

C_s	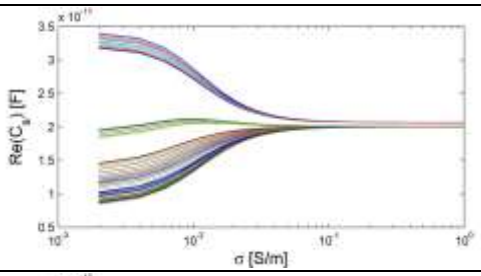	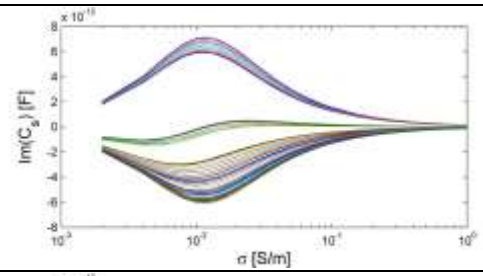
C_s - C_b	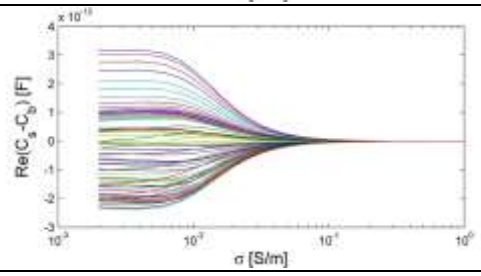	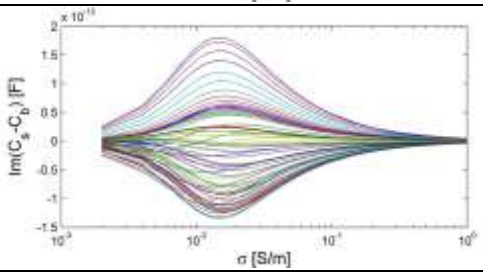

Table 2. 2-norm value of real and imaginary part of each set of capacitance over one conductivity

Capacitance	Real part	Imaginary part
C_b	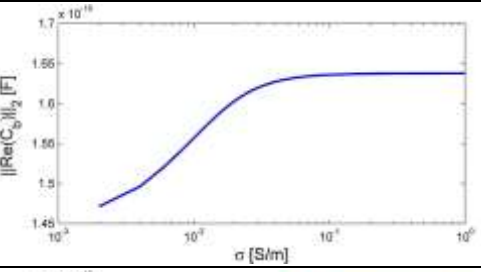	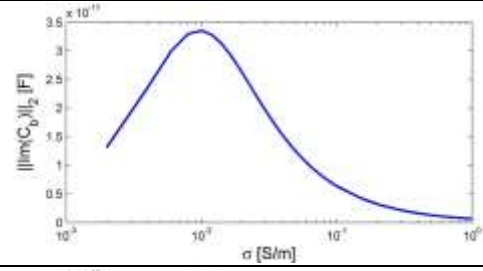
C_s	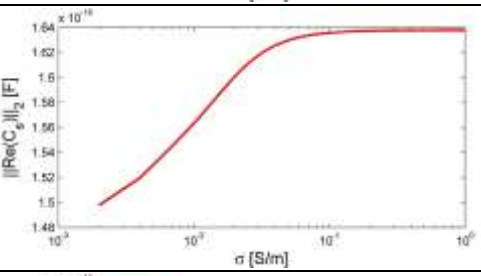	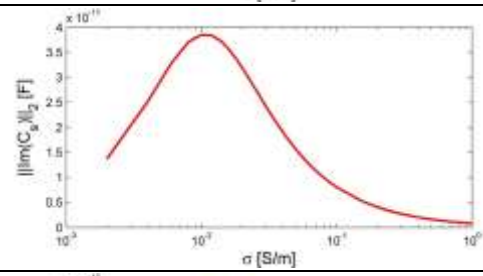
C_s - C_b	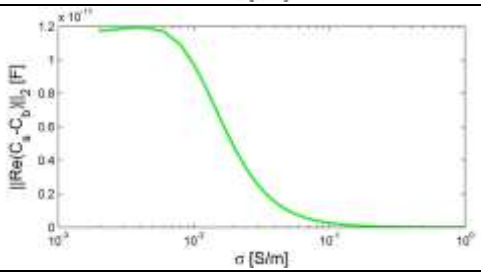	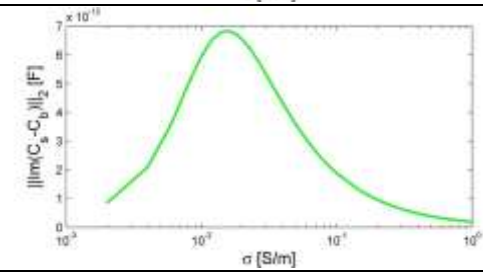

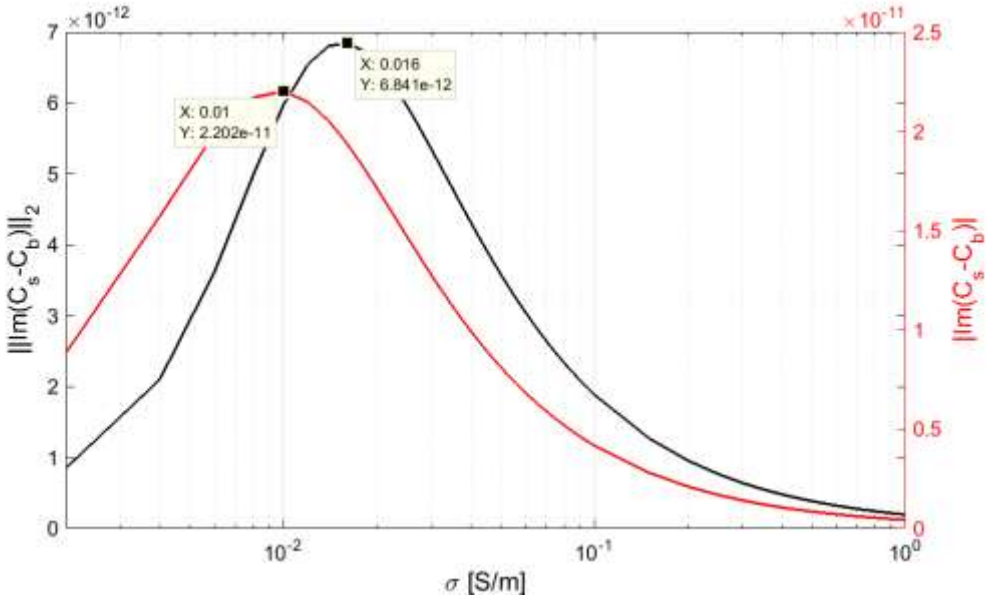

Figure 3. Comparison in imaginary part of the capacitance: 2-D simulation *verse* 1-D analysis.

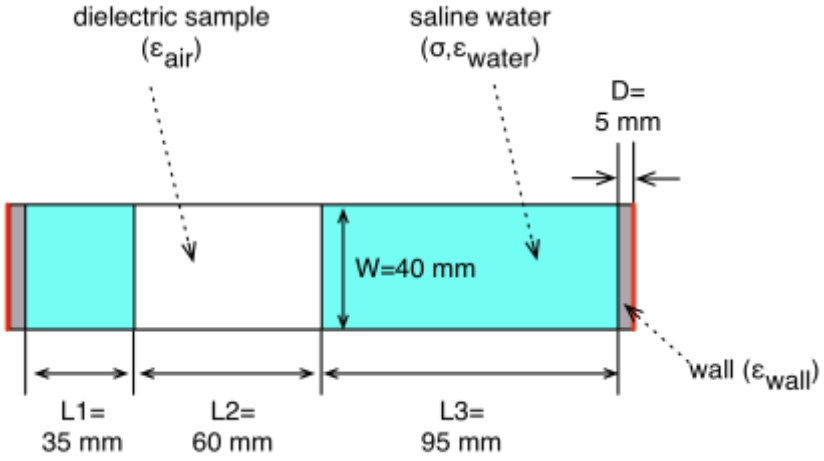

Figure 4. 1-dimensional analytical model

In **Table 2,** for the real part of the difference, the value becomes relatively small when the conductivity is higher than 0.1 S/m. The magnitude of the imaginary part reaches a peak around $\sigma = 0.016$ S/m then declines, as the black line shown in **Figure 3**. To have a better understanding of this peak value, we downgrade the 2-D problem to a one dimensional model and use parallel electrodes to calculate the complex capacitance, as shown in Figure 4. The Size of the electrode (the red line in **Figure 4**) is the same as the 2-D model, since it is not a 3-D model, the length of the electrodes is considered as a unit length. By applying the value of dimensions and permittivity into the **equation (9)** and increasing the conductivity of the water, the red line in **Figure 3** is obtained.

$$C_s - C_b = \frac{1}{\frac{2}{\varepsilon_{wall}A/D} + \frac{j\omega}{(\sigma + j\omega\varepsilon_{water})A}(\frac{1}{L_1} + \frac{1}{L_3}) + \frac{2}{\varepsilon_{air}A/L_2}} - \frac{1}{\frac{2}{\varepsilon_{wall}A/D} + \frac{j\omega}{(\sigma + j\omega\varepsilon_{water})A/(L_1 + L_2 + L_3)}} \quad \textbf{(9)}$$

Comparing the plots in **Figure 3**, the peak value of 1-D model locates at $\sigma = 0.010\ \mathrm{S/m}$, which is still not the same as $\sigma = 0.016\ \mathrm{S/m}$ in the 2-D simulation, since the complexity of the 2-D geometric distribution makes the this difference. But it shows that both 2-D and 1-D calculation have a similar trend with increasing conductivity of water.

From this simulation, the measurement of complex capacitance tends to decrease, when the conductivity increases. Theoretically, the conductivity makes the added sample "invisible" from measurement reading in both real and imaginary parts.

3.2 Complex permittivity reconstruction

In the consideration of the experiment speed, the sensing region is divided into a coarse mesh of 920 elements as shown in **Figure 2(b)** for faster image reconstruction. The real and imaginary parts of change in complex permittivity distribution are calculated by modified Tikhonov regularization according to **equation (8)** and are plotted separately in **Table 4**. The value of the imaginary part of change in complex permittivity, $\Delta\varepsilon_i$, is converted into the format of conductivity by multiplying the angular frequency, $2\pi f$.

To demonstrate the reliability of the reconstruction, we add noise onto the capacitances to simulate the inaccuracy in measurement. The noise added affects both the magnitude and the phase angle of the complex capacitances. For an impedance analyser, the accuracy of the phase angle measurement normally equals 1% of the one on the magnitude, for example the 4990A impedance analyser from Keysight Technologies [20]. The noisy capacitance is set as the equation below:

$$C = |C|\angle\theta \quad \textbf{(10)}$$

$$C_{noise} = (1 + e)|C|\angle(1 + \frac{e}{100})\theta \quad \textbf{(11)}$$

$$-E < \mathrm{random}(e) < E \quad \textbf{(12)}$$

Where C is the noise-free capacitance between one pair of electrodes, θ is the phase angle of C and e is the noise randomly generated and within the controlled level of E. The noise level is chosen at E=2%.

Table 3. Image reconstructed from simulated data

		$\Delta\varepsilon$		$\Delta\sigma$	
	Real distribution	**Noise free**	**2% free**	**Noise free**	**2% free**
One sample		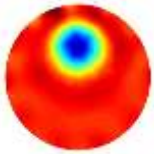	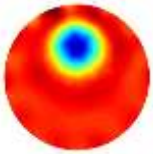	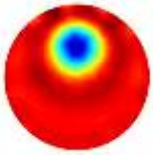	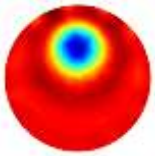
Two samples		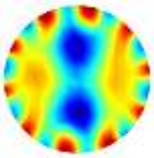	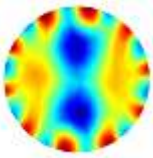	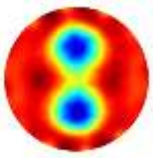	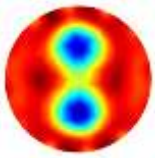
Annular air		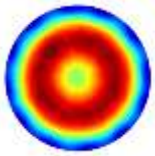	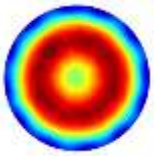	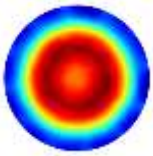	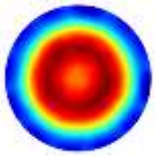
Annular water		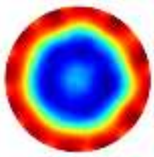	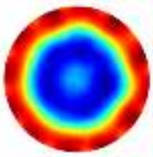	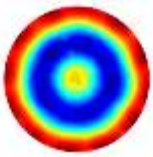	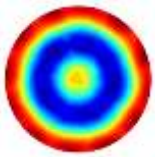
Stratified					

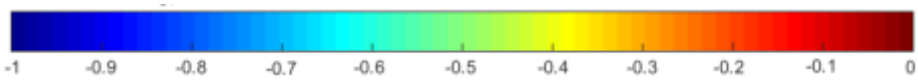

Table 3 shows the simulation results of different distributions. In the column of "Real Distribution", the blue region stands for water of relative permittivity of 80 and conductivity of 0.01 S/m; the white region stands for air of relative permittivity of 1 and conductivity of 0. The background data is taken when the sensor is filled with conductive water, so air sample added will result in a drop on permittivity and conductivity distribution on the area of air exists. Thus the reconstructed distribution is in negative value. Except for imaging several different scenarios of fixed conductivity, the same scenario of different conductivity is also worth studying. One circular sample of air adding into conductive water is studied by increasing the conductivity of water. The results are reconstructed in **Table 4**.

When the capacitance data used is noise-free (the plots in the second and forth column of **Table 4),** the reconstruction of either permittivity or conductivity is stable, which distinguishes air (low-permittivity and non-conductivity) from water in the sensor. However when the conductivity is higher than 0.26 S/m, the permittivity plot starts decaying. When the data contains noise (2%), this causes the increasing instability in reconstructions (the plots in the third and fifth column of **Table 4**). With simulations

of a pre-set distribution of ε and σ, we can tell the accuracy of the reconstruction directly by the images. However, for a real test of unknown distribution, the unpredictable noise in the measurements result in the inaccuracy of the images. Therefore, a parameter is proposed to measure the stability of calculated distribution of both permittivity and conductivity. The value α in red shown in the tables is the regularisation factor applied to the Tikhonov algorithm.

Set the conductivity of the background at σ, then solve the inverse problem for *N* times under different random noise within the same level. And we got *N* sets of the distribution of the electric permittivity change, $\Delta\varepsilon_n$. Then normalise $\Delta\varepsilon_n$ to the range from 0 to1, as shown in equation (13):

$$x_n = \frac{\Delta\varepsilon_n - \min(\Delta\varepsilon_n)}{\max(\Delta\varepsilon_n) - \min(\Delta\varepsilon_n)} \qquad for\ n = 1,2,\cdots,N \tag{13}$$

Then we calculate the correlation coefficients, $Corr_n$, between $x_n$and x_{n+1}:

$$Corr_n = \frac{\sum_{n=1}^{N}(x_{n+1} - \overline{x_{n+1}})\,((x_n - \overline{x_n}))}{\sqrt{\sum_{n=1}^{N}(x_{n+1} - \overline{x_{n+1}})^2}\sqrt{\sum_{n=1}^{N}(x_n - \overline{x_n})^2}} \tag{14}$$

As a result, *(N-1)* correlation coefficients are obtained and the mean value of them is the proposed stability parameter. The stability parameters for the simulated data of different conductivity represents the reliability of the reconstructed images on the similar real experiments, so we call it the reliability parameter, ***R***.

$$\boldsymbol{R} = \frac{1}{N-1} * \sum_{n=1}^{N-1} Corr_n \tag{15}$$

In this experiment, *N* equals 100 to make sure enough random noise for data samplling. We calculate the reliability parameters for the conductivity from 0.001 to 0.6 S/m and the plots of calculated conductivity and permittivity distributionsare shown below.

Table 4. Reconstruction of calculated $\Delta\boldsymbol{\varepsilon}$ and $\Delta\boldsymbol{\sigma}$ distribution

$\boldsymbol{\sigma}$ $[\boldsymbol{S/m}]$	$\Delta\boldsymbol{\varepsilon}$		$\Delta\boldsymbol{\sigma}$	
	Noise-free	**2% Noise**	**Noise-free**	**2% Noise**
0.001 α =1e-7	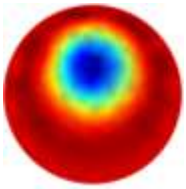	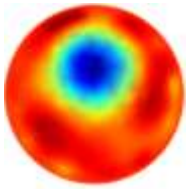	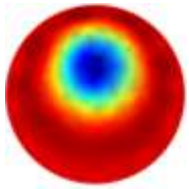	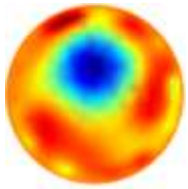
0.01 α =1e-8	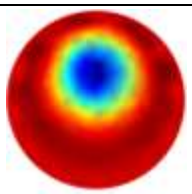	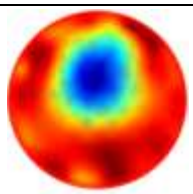	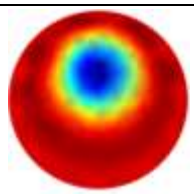	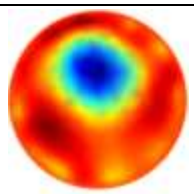
0.015 α =5e-9	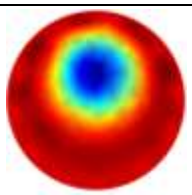	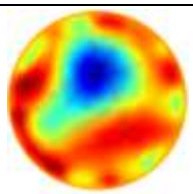	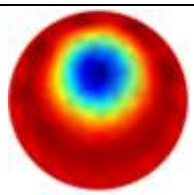	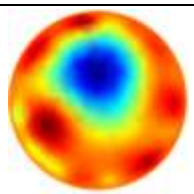
0.02 α =5e-9	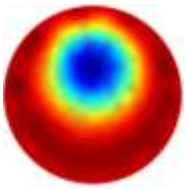	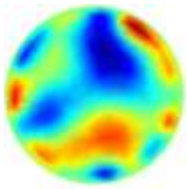	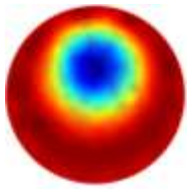	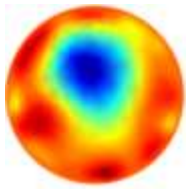
0.1 α =1e-11	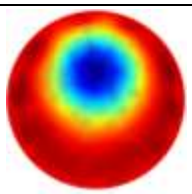	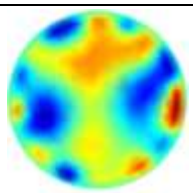	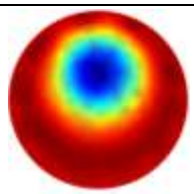	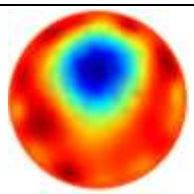
0.26 α =2.5e-13	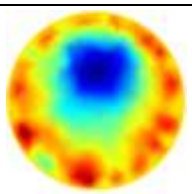	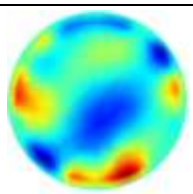	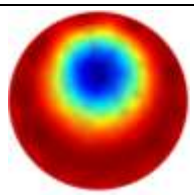	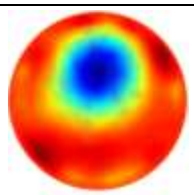
0.6 α =1e-14	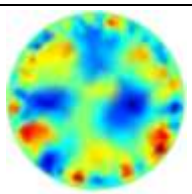	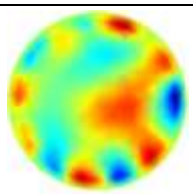	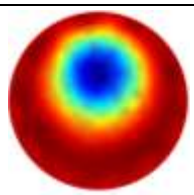	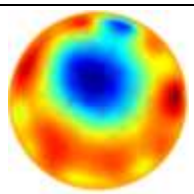

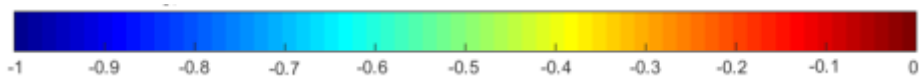

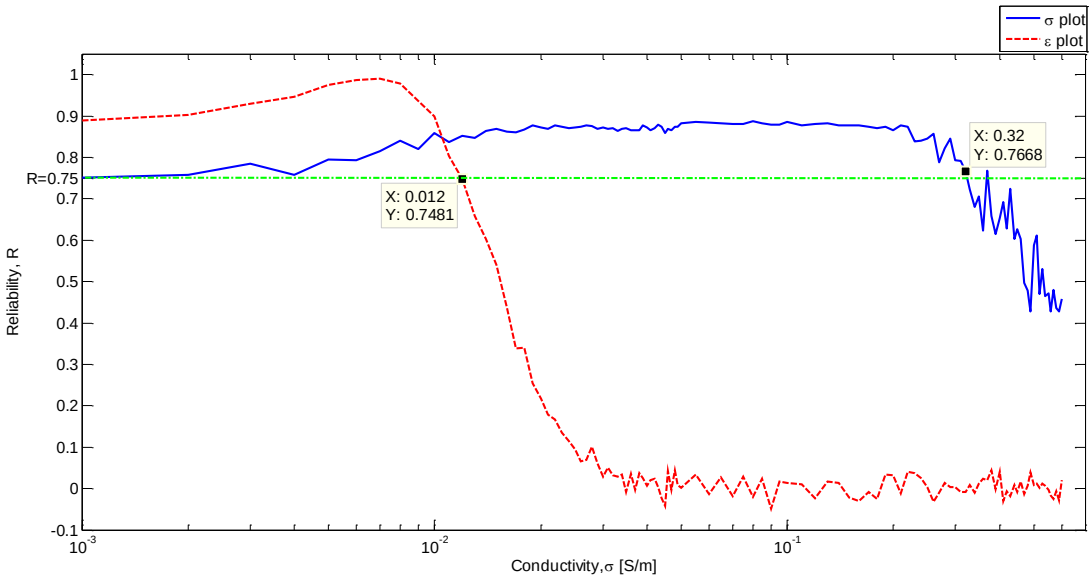

Figure 5. Reliability values of the noisy data for increasing conductivity**.**

From our experimental observation in this case, we found that above the green dashed line, *i.e.*, ***R>0.75***, the reconstructed images are relatively reliable. In other words, in the case of this simulation scenario, when the conductivity is higher than 0.32 S/m and 0.012 S/m, the σ plot and ε plot are not reliable respectively.

The results indicate that simultaneous reconstruction of both the permittivity and conductivity is feasible but limited to a small range of conductivity. In this section, the simulation model incorporates an air inclusion in the water background. This means that the admittance data simulated between the electrodes contains information about the changes in both permittivity and conductivity due to the air. Two factors changing increases the complexity of verifying this simultaneous reconstruction. To verify this method, two hypothetical inclusions are proposed in the next section, and the effect of the frequency is investigated.

3.3 Multiple frequency ECT

In this section the effect of changes in permittivity or conductivity distribution on the simultaneous reconstruction is investigated. A sample with high conductivity but low permittivity (like "conductive gas") is used to test the permittivity (ε) plot and a sample of low conductivity but high permittivity (such as deionised water) is used to test the conductivity (σ) plot. The size and location information is presented in **Table 5**. The simulations is done with 5 frequencies: 125 kHz, 625 kHz, 1.25 MHz, 6.25 MHz and 12.5 MHz. The background measurement is taken when the sensing region is filled with only sample 3.

Table 5. Three cases of different electric property and positions for simulations

No. of the sample	Radius and location	Relative permittivity	Conductivity (S/m)
1 (Grey)	R=3 cm centered at(0,4) cm	1	0.05
2 (Green)	R=3 cm centered at(0,-4) cm	80	0
3 (Blue)	R=9.5 cm centered at (0,0) cm	80	0.05

Case1	Case 2	Case 3
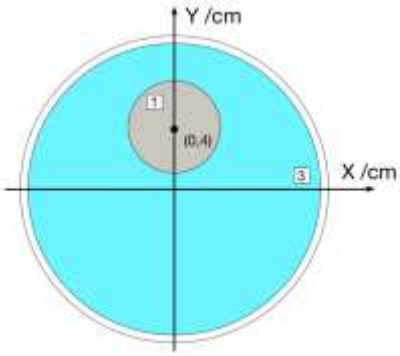	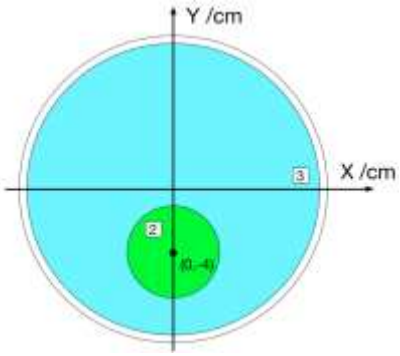	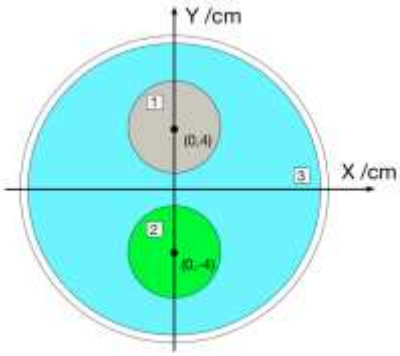

Under different frequency, the measurement of capacitance is influenced by adding sample to different extent. The 2-norm values of the noise-free capacitance difference, ΔC, are listed in **Table 6** and the ones with 2% noise, ΔC_e, are in **Table 7**.

Table 6. The change in noise-free capacitance difference in Case 1, 2& 3.

Case	ΔC	125 kHz	625 kHz	1.25 MHz	6.25 MHz	12.5 MHz
1	$\|\|Re(\Delta C)\|\|_2$	1.933e-15	4.751e-14	1.804e-13	1.109e-12	1.295e-12
	$\|\|Im(\Delta C)\|\|_2$	5.744e-17	7.091e-15	5.457e-14	2.807e-12	6.096e-12
2	$\|\|Re(\Delta C)\|\|_2$	2.262e-14	5.454e-13	1.960e-12	7.256e-12	3.255e-12
	$\|\|Im(\Delta C)\|\|_2$	4.183e-13	1.984e-12	3.376e-12	2.264e-12	3.970e-12
3	$\|\|Re(\Delta C)\|\|_2$	2.133e-14	5.144e-13	1.851e-12	7.159e-12	4.261e-12
	$\|\|Im(\Delta C)\|\|_2$	4.183e-13	1.991e-12	3.429e-12	2.464e-12	5.739e-12

Table 7. The change in capacitance difference with 2% noise in Case 1, 2& 3.

Case	ΔC_e	125 kHz	625 kHz	1.25 MHz	6.25 MHz	12.5 MHz
1	$\|\|Re(\Delta C_e)\|\|_2$	2.455e-12	2.678e-12	2.603e-12	2.656e-12	2.797e-12
	$\|\|Im(\Delta C_e)\|\|_2$	1.969e-14	1.010e-13	2.015e-13	2.884e-12	6.116e-12
2	$\|\|Re(\Delta C_e)\|\|_2$	2.560e-12	2.517e-12	3.177e-12	7.446e-12	4.080e-12
	$\|\|Im(\Delta C_e)\|\|_2$	4.100e-13	1.994e-12	3.384e-12	2.313e-12	3.879e-12
3	$\|\|Re(\Delta C_e)\|\|_2$	2.584e-12	2.487e-12	3.126e-12	7.477e-12	4.827e-12
	$\|\|Im(\Delta C_e)\|\|_2$	4.170e-13	2.001e-12	3.418e-12	2.515e-12	5.724e-12

The 2% of noise will have an impact on the capacitance difference shown above. And it can be quantified by the change rate between the numbers in **Table 6** and **Table 7**. The change rate is defined as equation below and filled in **Table 8**:

$$Change\ rate = \frac{\|\boldsymbol{Re}(\Delta \boldsymbol{C_e})\|_2}{\|\boldsymbol{Re}(\Delta \boldsymbol{C})\|_2} - 1 \quad or \quad \frac{\|\boldsymbol{Im}(\Delta \boldsymbol{C_e})\|_2}{\|\boldsymbol{Im}(\Delta \boldsymbol{C})\|_2} - 1 \qquad \textbf{(16)}$$

These CRs demonstrate that in all the three cases the real part of the capacitance difference is affected by the noises significantly in lower frequency as well. The imaginary part is immune to this 2% noise for all frequencies for **case 2** and **3**.

Table 8. The change rate between ΔC and ΔC_e

Case	Change rate	**125 kHz**	**625 kHz**	**1.25 MHz**	**6.25 MHz**	**12.5 MHz**
1	Real	1269.046	55.367	13.429	1.395	1.160
	Imaginary	341.792	13.243	2.692	0.027	0.003
2	Real	112.174	3.614	0.621	0.026	0.253
	Imaginary	-0.019	0.005	0.002	0.021	-0.023
3	Real	120.143	3.834	0.689	0.044	0.133
	Imaginary	-0.003	0.005	-0.003	0.021	-0.003

Then in **Table 9** and **Table 10**, the reconstructions of $\Delta\varepsilon$ and $\Delta\sigma$ change based on the capacitance with or without noise are shown.

Table 9. Reconstruction of $\Delta\boldsymbol{\varepsilon}$ and $\Delta\boldsymbol{\sigma}$ distribution in Case 1&2

Frequency	Noise level	Case 1		Case 2	
		$\Delta\varepsilon$	$\Delta\sigma$	$\Delta\varepsilon$	$\Delta\sigma$
125kHz α =1e-13	0	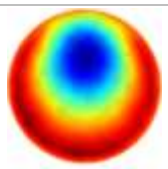	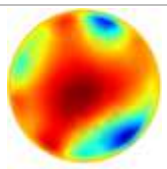	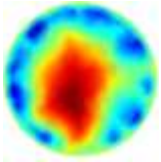	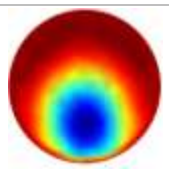
	2%	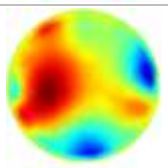	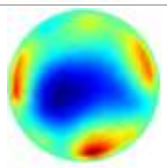	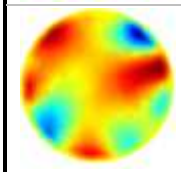	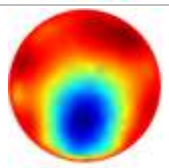
625kHz α =1e-11	0	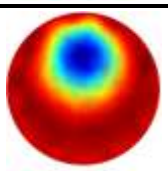	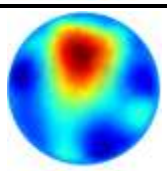	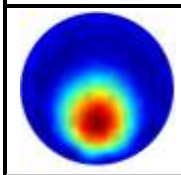	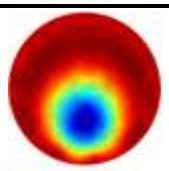
	2%	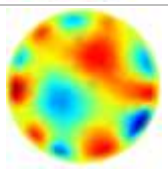	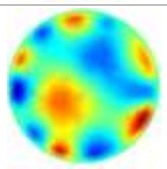	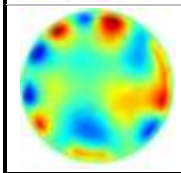	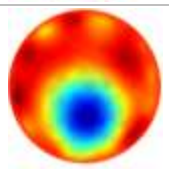
1.25MHz α =1e-10	0	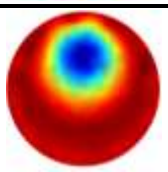	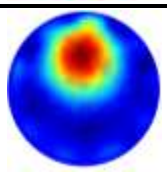	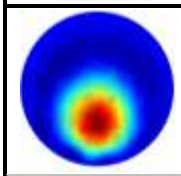	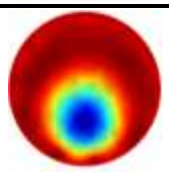
	2%	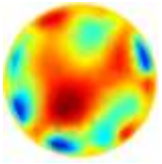	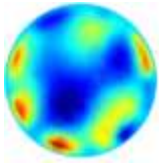	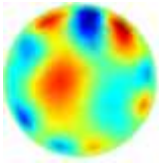	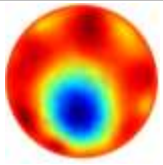

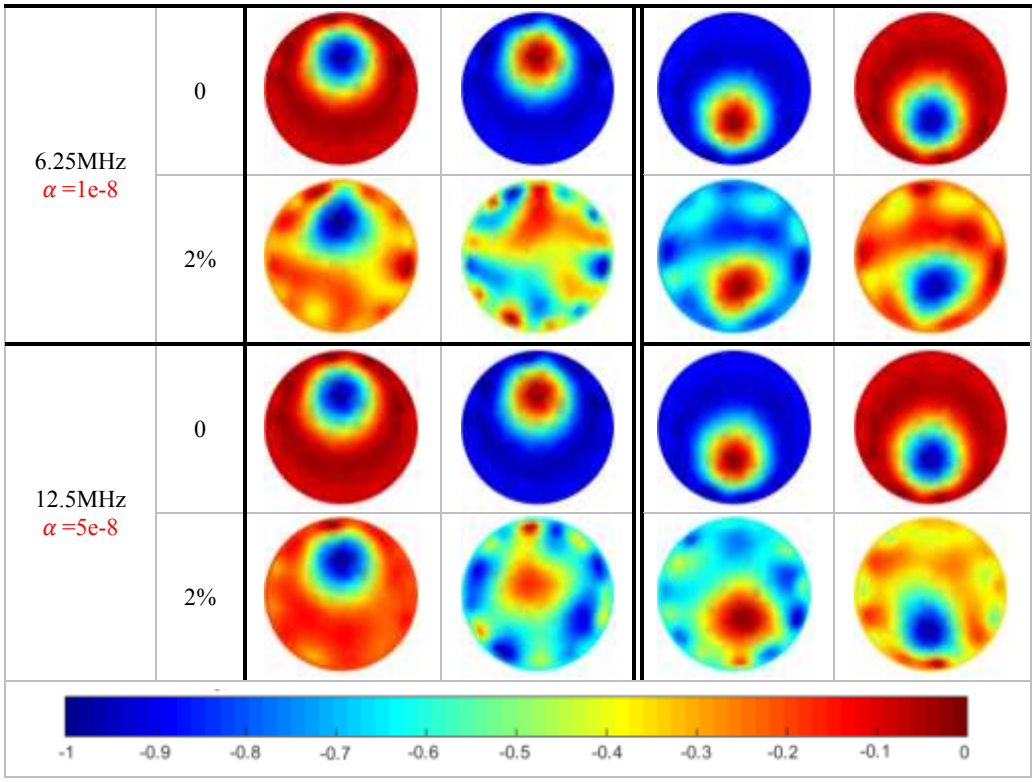

Table 10. Reconstruction of $\Delta\boldsymbol{\varepsilon}$ and $\Delta\boldsymbol{\sigma}$ distribution in Case 3

Frequency	Noise level	Case 3	
		$\Delta\varepsilon$	$\Delta\sigma$
125kHz α =1e-13	0	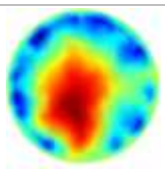	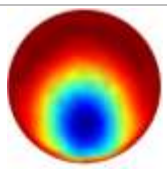
	2%	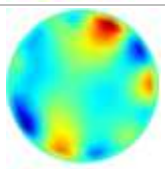	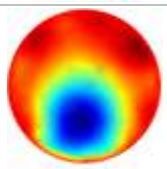
625kHz α =1e-11	0	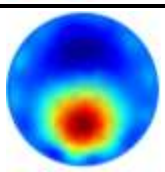	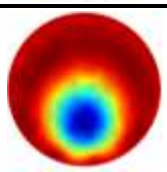
	2%	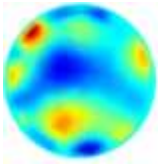	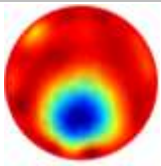
1.25MHz α =1e-10	0	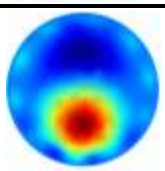	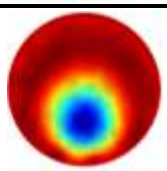

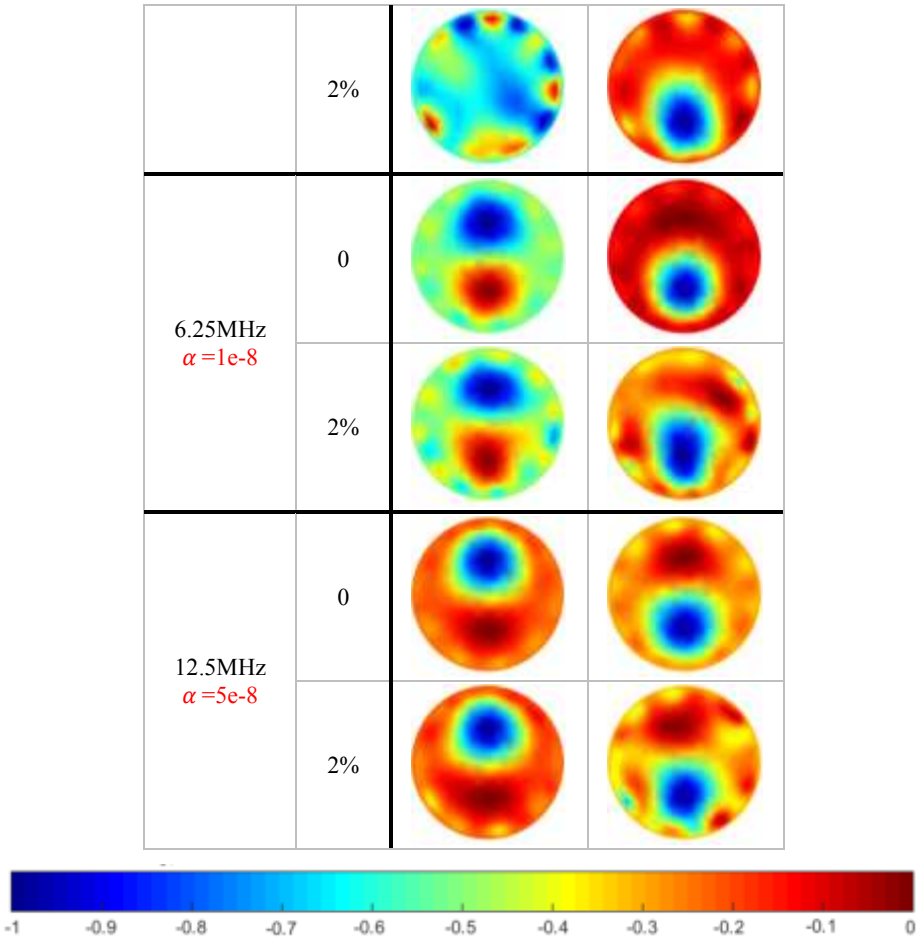

To give a clear view of the reliability of the images in tables above, the same evaluation process as in section 3.2 was conducted on the data with 2% noise. The reliability parameter of different frequencies and cases is plotted below:

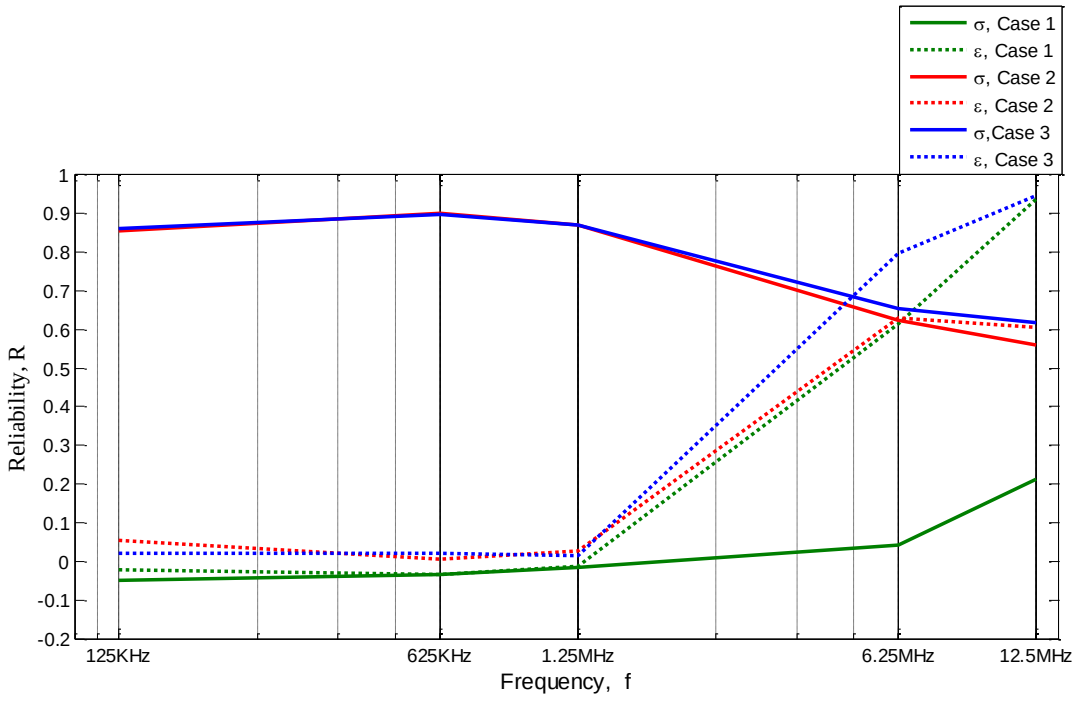

Figure 6. Reliability plot of the noisy data along the increasing conductivity.

1. In Case 1, the noise-free data illustrates that the permittivity change, which results from replacing conductive water with a "conductive gas", has more impact on the real part of ΔC in the frequency range from 125 kHz to 1.25 MHz, *i.e.*, the real part is much bigger than the imaginary part. Within this range the noise makes a significant impact on both real and imaginary parts of ΔC, as shown by the images in **Table 9**. When the frequency keeps increasing, the imaginary part of the ΔC becomes bigger than the real part, and the effect of noise on the value of ΔC becomes minor. As shown in the rows 6.25 MHz and 12.5 MHz in **Table 9**, the ε images of the noisy data performs similarly to the noise-free data, and the reliability of it increases (the green dot line in **Figure 6**).

2. In Case 2, as frequency grows, influence on the real part of ΔC from the noise trends smaller, while the imaginary part of ΔC is immune to the noise, and has only a very small perturbation. From the reconstruction in **Table 9**, a reliable performance over noise and different frequencies of the σ images is observed (the red solid line in **Figure 6**).

3. In Case 3, both permittivity and conductivity affect the measurements simultaneously. However the measurements of the frequencies from 125 kHz to 1.25 MHz are close to the value in Case 2, which means the conductivity difference from the deionised water to conductive water has a dominant impact, therefore the images in **Table 10** is similar to Case 2 at the same frequency range. Thereafter, at higher frequency the impact on capacitance from "conductive gas" increases and in **Table 10**, the blue phantom on images of both ε and σ illustrates the two inclusions respectively. And the reliability of the images are plotted as the blue lines in **Figure 6.**

In **Table 6** and **Table 8**, a small capacitance difference of noise free scenario in low frequency is significantly influenced by the added noise. Therefore in Case 1, where a small capacitance difference is only caused by a regional permittivity change, the reconstruction failed due to the added noise. While in Case 2, the impacts from the regional conductivity change is much bigger and not sensitive to the noise. For the same size of these two samples taking over the place of the background water, the magnitude of the local impacts can only be the same when the change in permittivity equals the change in conductivity divided by angular frequency:

$$|\varepsilon_{water} - \varepsilon_{air}| = \left|\frac{\sigma_{water}}{2\pi f}\right| \quad \textbf{(17)}$$

Where ε_{water} and σ_{water} are the permittivity and conductivity of water, and ε_{air} is the permittivity of air. In our cases, as the setting in **Table 5**, only when frequency equals $f = \left|\frac{\sigma_{water}}{2\pi(\varepsilon_{water}-\varepsilon_{air})}\right| = 11.377$ MHz, the two type of samples have the same magnitude of influence. This explains that in case 3, when frequency higher than the

6.25 *MHz*, the permittivity image starts working, since the weighting of permittivity change's impact is not negligible compared with conductivity change.

4. Discussion

Traditional ECT has been used as a method to image permittivity distribution of dielectric samples for a long time. This paper presented an in depth evaluation of using the contactless capacitive method to monitor the electric property change, and to reconstruct the permittivity and conductivity in one go. Both real and imaginary parts of the complex permittivity are investigated through modelling. In section 3.3, the hypothetical samples provides a preliminary understanding about the influence on measurements and reconstruction from permittivity change and conductivity change. In the real experiment, such as oil/gas/water phase flow imaging, the low permittivity components are always low conductivity. Theoretically, the simultaneous reconstruction provides more information of both permittivity and conductivity distribution from sets of admittances (complex value) data. From the simulations of the conductive water background, we found that the conductivity plots have very reliable performance in showing the low-conductive inclusion, even though the image of permittivity fails. This means that the conductivity plots can be used as prior information for iterative algorithms.

The conductivity and frequency jointly affects the measurement of the complex capacitance as expressed in **equation (2)**, applying higher excitation frequency to ECT measurement would help to generate better images of both ε and σ distribution. Particularly in the case of the non-conductive inclusions staying in the conductive background, increasing frequency of excitation signal has the same result of decreasing the conductivity of the background. More experimental work on different frequencies will be carried out based on an impedance analyser, instead of a purely capacitance measurement unit. Therefore, the feasibility of the multi-frequency complex admittance ECT method will be tested in future.

5. Conclusions

By using capacitance measurements between the electrodes at the periphery of flow pipe, ECT visualises the permittivity distribution of multi-phase flow. This is useful for cases such as gas-oil or solid-gas flows, where the inclusions are normally dielectric or low-conductivity. For flows with a conductive medium, such as conductive water, the conductivity will affect the capacitance measurements. The forward model and inverse solver of conventional ECT also cannot analyse this effect correctly from the measurements, so ECT fails to work. If the measurements for ECT are the admittance including both capacitance and resistance, with a complex-value sensitivity map, a simultaneous reconstruction of permittivity and conductivity is

possible as proposed in this paper. A realistic noise model presented to evaluate how each of the complex-value capacitance components in a variety of frequencies contributes to imaging permittivity and conductivity. The results of this paper demonstrate a much greater potential for ECT as a far more versatile imaging device than it is currently perceived as. The contactless nature of ECT makes this device potentially suitable for many new application areas such as medical imaging and process monitoring with a conductive medium.

References

1. Thorn, R., G.A. Johansen, and B.T. Hjertaker, *Three-phase flow measurement in the petroleum industry.* Measurement Science and Technology, 2013. **24**(1): p. 012003.

2. Huang, S., et al., *Capacitance-based tomographic flow imaging system.* Electronics letters, 1988. **24**(7): p. 418-419.

3. Li, Y., et al., *Gas/oil/water flow measurement by electrical capacitance tomography.* Measurement Science & Technology, 2013. **24**(7).

4. Chaminda, P., et al., *Electrical capacitance tomography (ECT) and gamma radiation meter for comparison with and validation and tuning of computational fluid dynamics (CFD) modeling of multiphase flow.* Measurement Science and Technology, 2014. **25**(7): p. 075404.

5. Hjertaker, B.T., R. Maad, and G.A. Johansen, *Dual-mode capacitance and gamma-ray tomography using the Landweber reconstruction algorithm.* Measurement Science and Technology, 2011. **22**(10): p. 104002.

6. Hjertaker, B.T., et al., *Multimodality tomography for multiphase hydrocarbon flow measurements.* Sensors Journal, IEEE, 2005. **5**(2): p. 153-160.

7. Nowakowski, J., et al., *Multimodality measurement data fusion in image reconstruction for multiphase flow measurements.* Automatyka/Akademia Górniczo-Hutnicza im. Stanisława Staszica w Krakowie, 2010. **14**: p. 731-739.

8. Wang, B., Z. Huang, and H. Li. *Design of high-speed ECT and ERT system*. in *Journal of Physics: Conference Series*. 2009. IOP Publishing.

9. Zhang, M., L. Ma, and M. Soleimani, *Dual modality ECT–MIT multi-phase flow imaging.* In press, Flow Measurement and Instrumentation, 2015.

10. Ma, L., A. Hunt, and M. Soleimani, *Experimental evaluation of conductive flow imaging using magnetic induction tomography.* International Journal of Multiphase Flow, 2015. **72**(0): p. 198-209.

11. Griffiths, H., et al., *Residual capacitive coupling and the measurement of permittivity in magnetic induction tomography.* Physiological measurement, 2007. **28**(7): p. S301.

12. Korjenevsky, A. and T. Tuykin, *Experimental demonstration of electric field tomography.* Physiological measurement, 2010. **31**(8): p. S127.

13. Yang, C.L., et al., *Complex conductivity reconstruction in multiple frequency electrical impedance tomography for fabric-based pressure sensor.* Sensor Review, 2015. **35**(1): p. 85-97.

14. Liao, A. and Q. Zhou, *Application of ECT and relative change ratio of capacitances in probing anomalous objects in water.* Flow Measurement and Instrumentation, 2015. **45**(0): p. 7-17.

15. Li, Y. and M. Soleimani, *Imaging conductive materials with high frequency electrical capacitance tomography.* Measurement, 2013. **46**(9): p. 3355-3361.

16. Wang, B., et al., *Image reconstruction algorithm for capacitively coupled electrical resistance tomography.* Flow Measurement and Instrumentation, 2014. **40**(0): p. 216-222.

17. Wang, B., et al., *Modeling and optimal design of sensor for capacitively coupled electrical resistance tomography system.* Flow Measurement and Instrumentation, 2013. **31**(0): p. 3-9.

18. Wang, B., et al., *A Novel Electrical Resistance Tomography System Based on C4D Technique.* Instrumentation and Measurement, IEEE Transactions on, 2013. **62**(5): p. 1017-1024.

19. Hu, X. and W. Yang, *Planar capacitive sensors-designs and applications.* Sensor Review, 2010. **30**(1): p. 24-39.

20. *E4990A Impedance Analyzer Data Sheet*. 17 June 2015 [cited 2015 25 August]; Available from: http://literature.cdn.keysight.com/litweb/pdf/5991-3890EN.pdf.